

**Electronic Supplementary Information (ESI) for
Geometrical engineering of nearly fully cation-selective 2D angstrom-scale ionic diode
membranes for highly efficient osmotic energy conversion**

Amalia Rizki Fauziah,^a Rathi Aparna,^b Fery Prasetyo,^a Kalon Gopinadhan,^{b,c,}*

Li-Hsien Yeh^{a,d,}*

^a Department of Chemical Engineering, National Taiwan University of Science and
Technology, Taipei 10607, Taiwan

^b Department of Physics, Indian Institute of Technology Gandhinagar, Gujarat 382355, India

^c Department of Materials Engineering, Indian Institute of Technology Gandhinagar, Gujarat
382355, India

^d Advanced Manufacturing Research Center, National Taiwan University of Science and
Technology, Taipei 10607, Taiwan

*Corresponding Authors

Email: lhyeh@mail.ntust.edu.tw (Li-Hsien Yeh)

Email: gopinadhan.kalon@iitgn.ac.in (Kalon Gopinadhan)

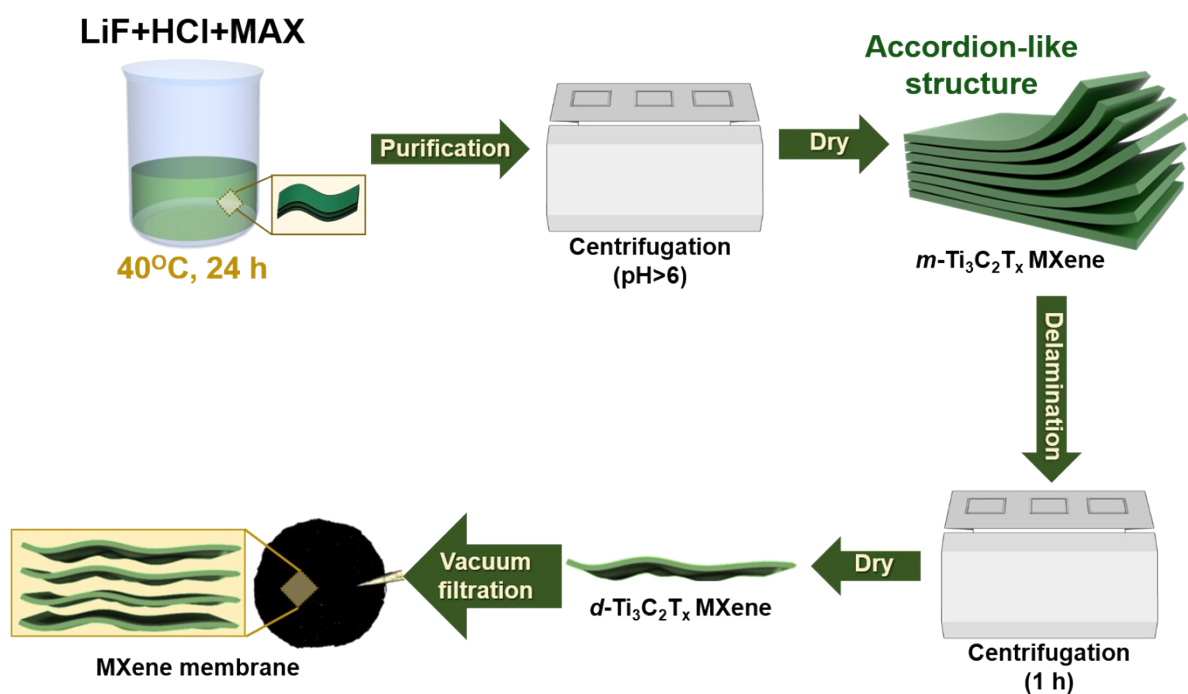


Fig. S1. Fabrication process flow depicting the preparation of MXene membrane.

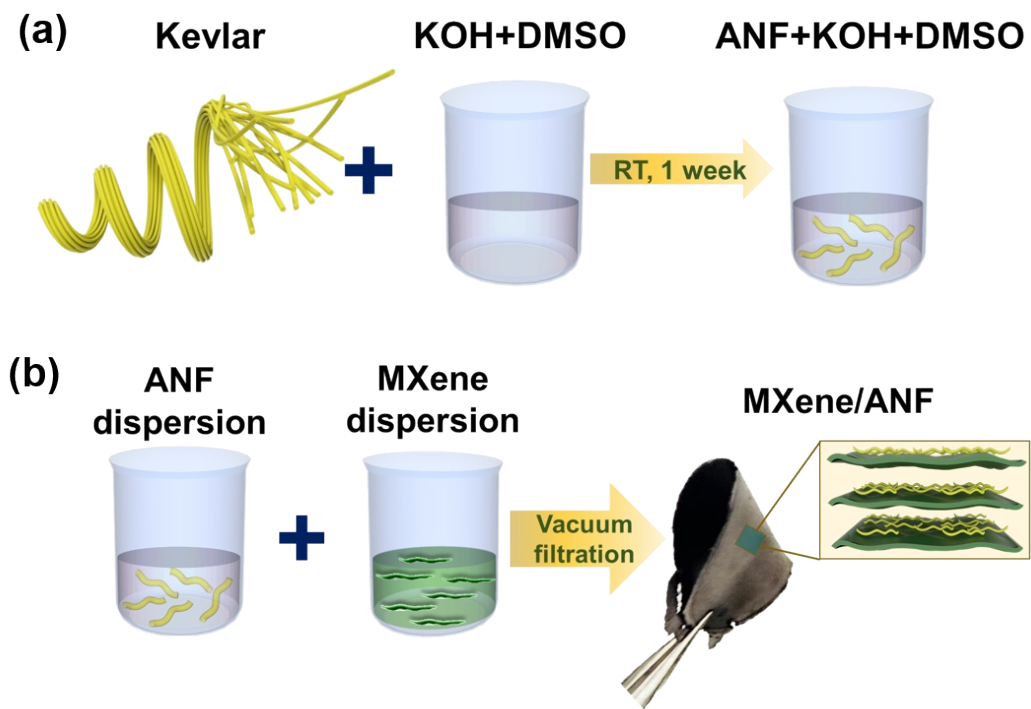


Fig. S2. Process diagram illustrating the fabrication of (a) ANF dispersion and (b) MXA (MXene/ANF) composite membrane.

Table S1. Preparation of MXAx composite membranes with varying ratios of MXene and

ANF.

Composite membrane	1 mg/mL MXene/H ₂ O (mL)	2 mg/mL ANF/DMSO (mL)
MXA ₀		0
MXA ₃	30	0.46
MXA ₅		0.80
MXA ₇		1.13

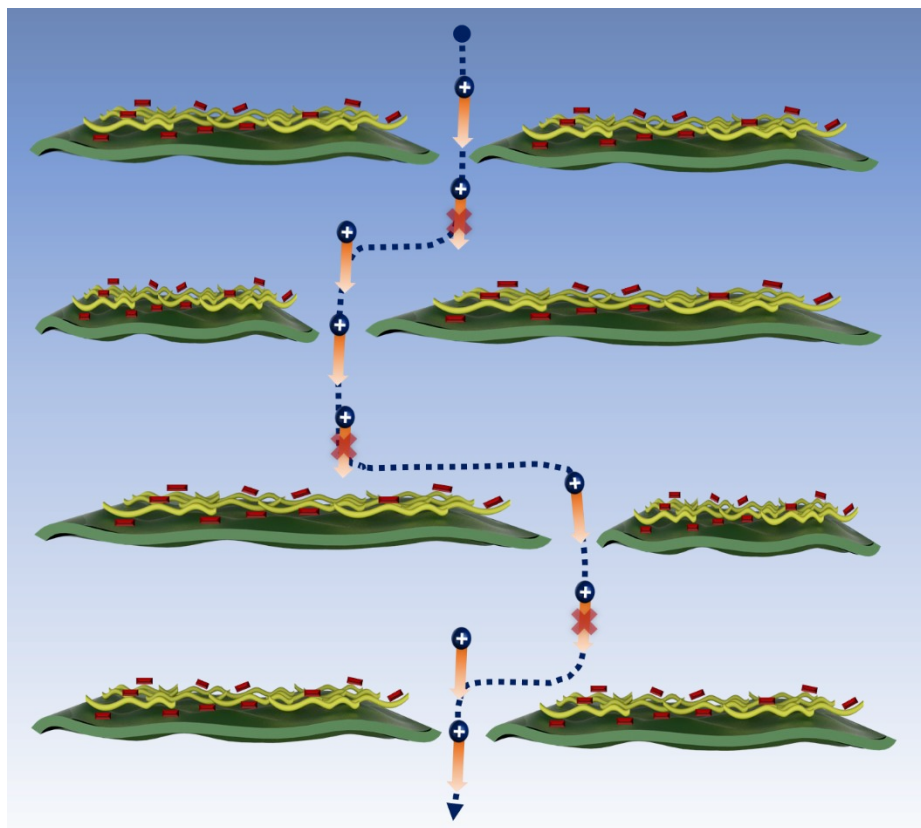


Fig. S3. The schematic illustration of tortuous ion pathways through an MXA in an out-of-plane orientation.

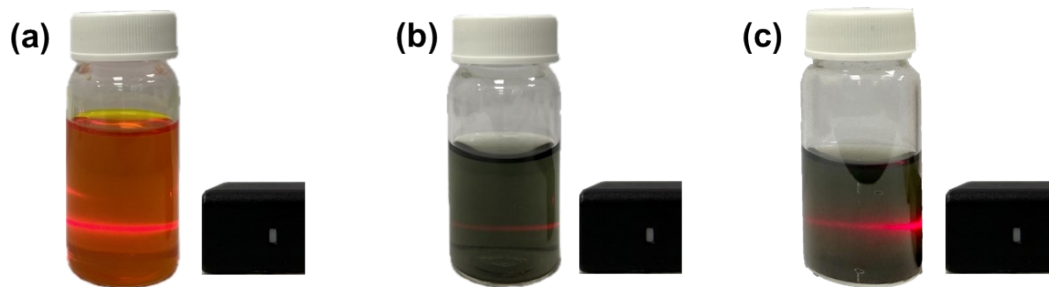


Fig. S4. The strong Tyndall effect of (a) ANF (in DMSO), (b) MXene (in water), and (c) MXA (in water/DMSO) dispersions.

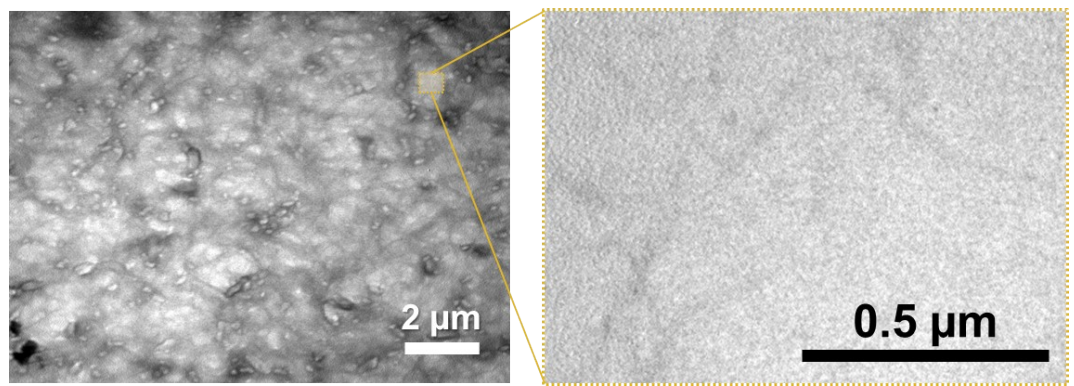


Fig. S5. The TEM image and its magnification (right-hand side) of ANF, verifying its clear fiber-like structure.

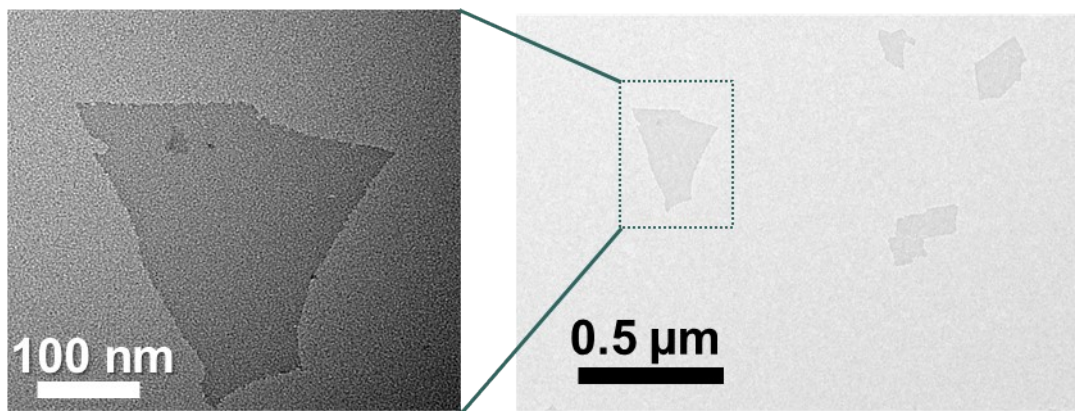


Fig. S6. The TEM image of MXene nanosheets, showing the ultrathin sheet structure.

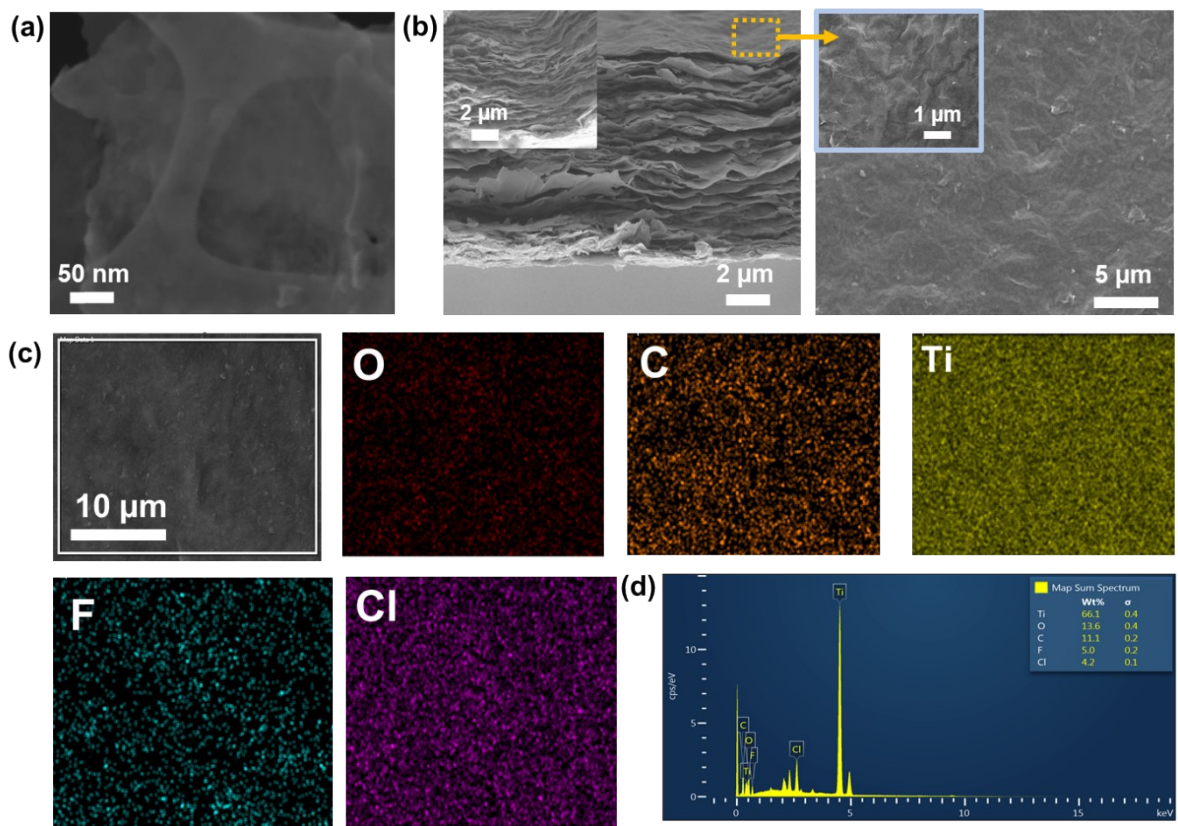


Fig. S7. (a) STEM image and (b) cross-section (left) and top (right) view SEM images of MXene. Insets in (b) indicate the magnified images. (c) Top-view SEM image and the corresponding elemental mappings of MXene membrane, showing the uniform distribution of titanium (Ti) elements across the MXene surface. (d) EDX spectrum of MXene.

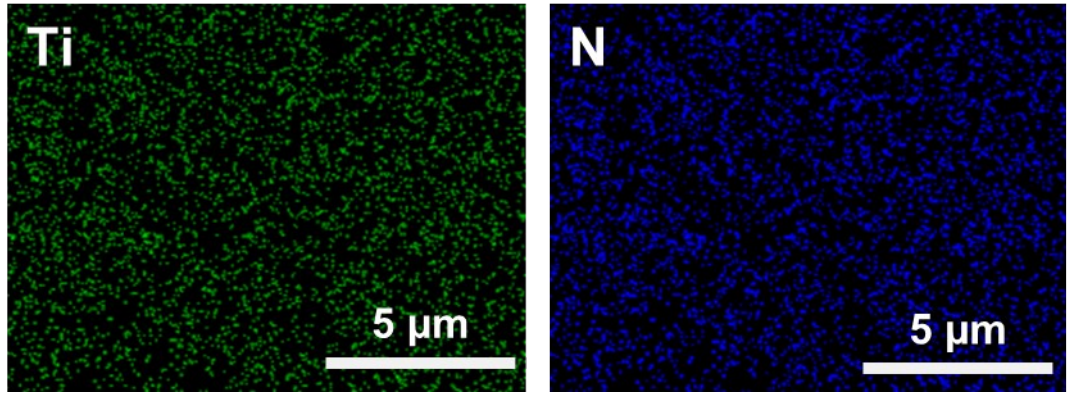


Fig. S8. EDX mapping analyses of the MXA membrane.

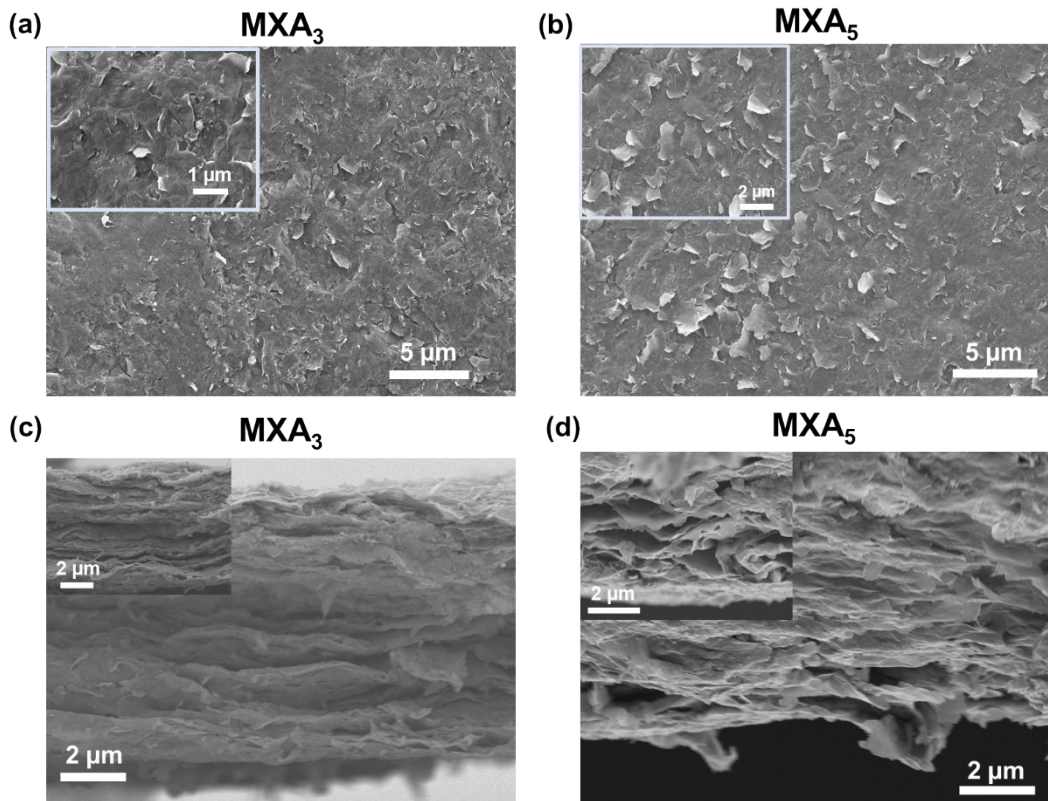


Fig. S9. (a)-(b) top view and (c)-(d) cross-section view SEM images of MXA membranes with various MXene/ANF compositions. All insets indicate magnified views.

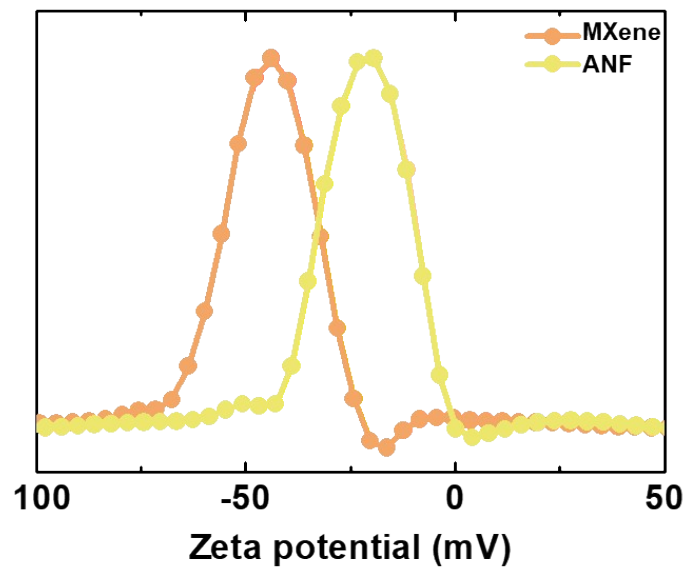


Fig. S10. Zeta potential measurements of the pristine MXene and ANF.

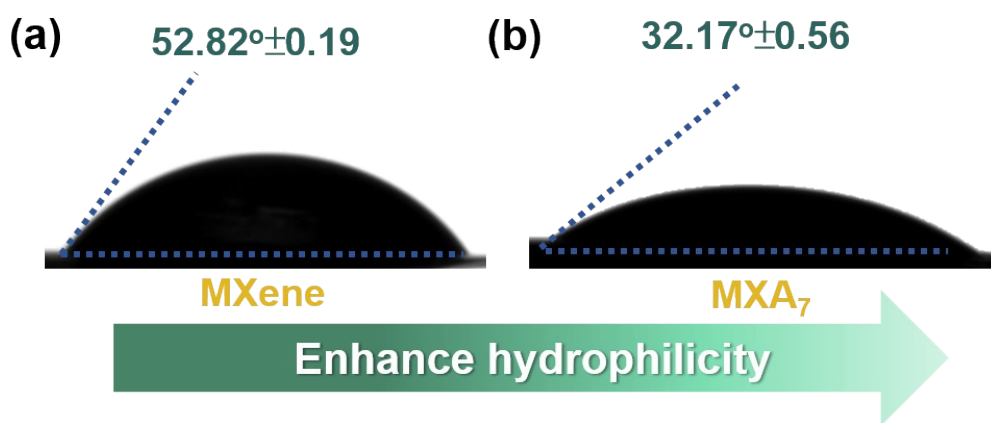


Fig. S11. Water contact angle measurements of (a) MXene and (b) MXA membrane.

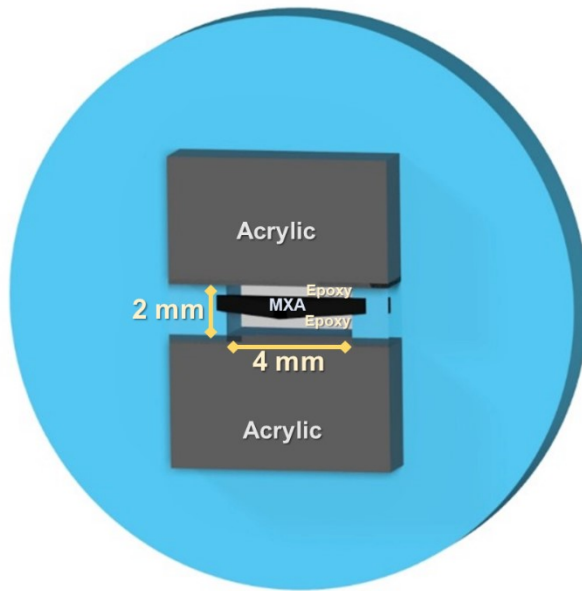


Fig. S12. Schematic of the experimental setup where the MXA membrane embedded in an epoxy-acrylic device.

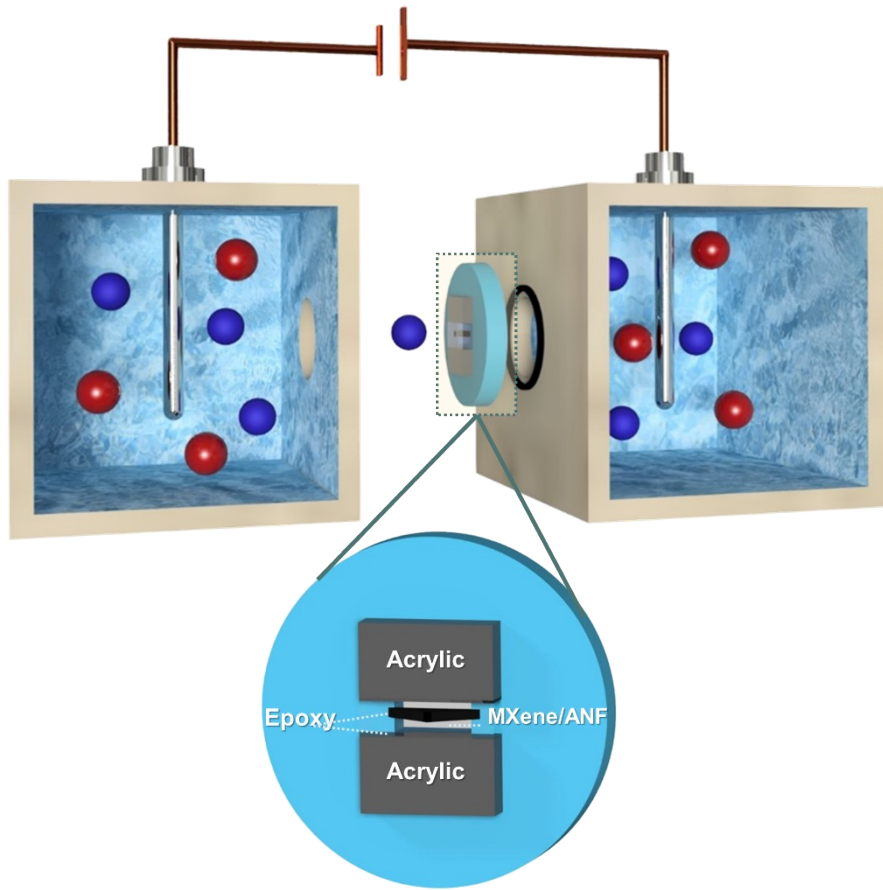


Fig. S13. The epoxy-acrylic device setup enabling in-plane ion transport through MXA composite membrane.



Fig. S14. Photograph of a large-scale MXA composite membrane in centimeter scale.

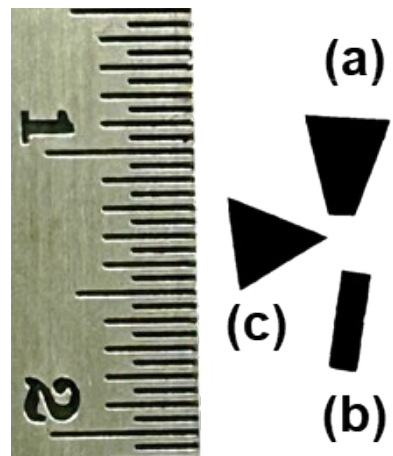


Fig. S15. Photographs of the geometrically engineered MXA membranes with (a) trapezoidal, (b) rectangular, and (c) triangular shapes.

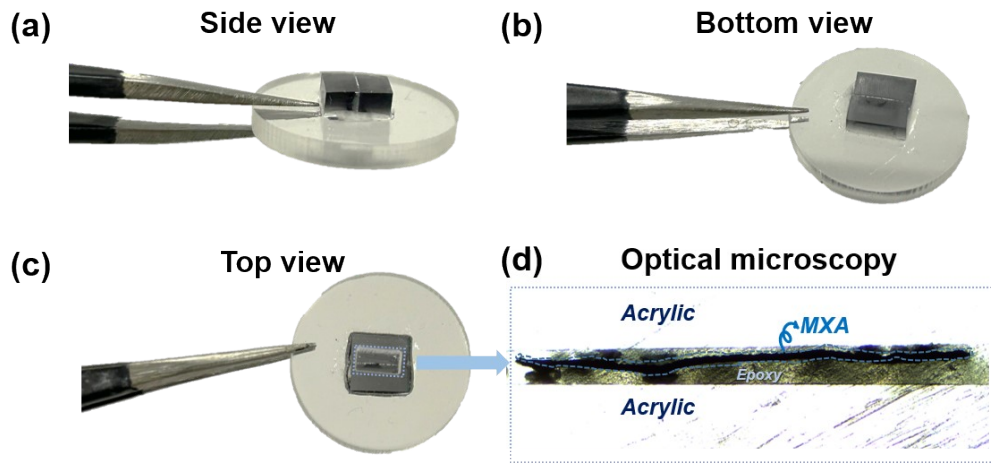


Fig. S16. The digital photographs of the MXA membrane embedded in the epoxy-acrylic device at different angles of (a) side, (b) bottom, and (c) top views. (d) The optical microscopy image of (c), showing that MXA membrane securely fixed between acrylic by epoxy.

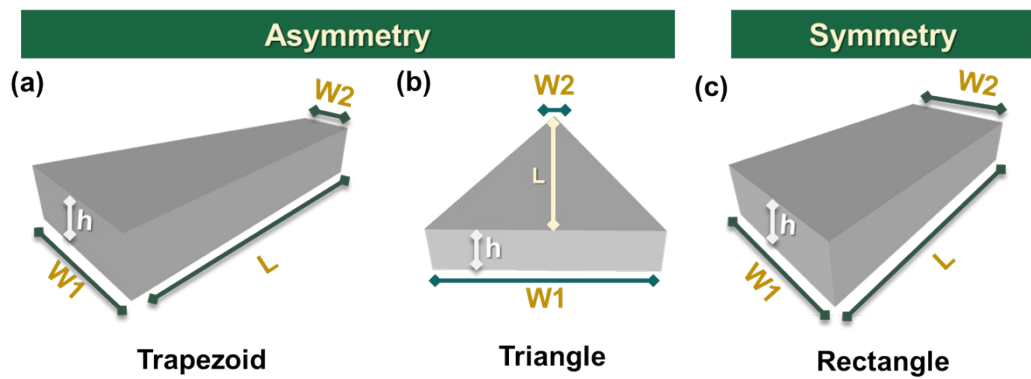


Fig. S17. Membrane geometries examined in the study: (a)-(b) asymmetric, (c) symmetric.

The membrane's dimension and effective testing area

The membrane geometry is shown in Fig. S17, with its dimensions listed in Table S2.

The effective ion transport area (A) corresponds to the smaller end of the membrane and is calculated as,

$$A = h \times W2 \quad (S1)$$

Table S2. The used MXA membranes with various geometries.

Geometry	W1 (mm)	W2 (mm)	Asymmetric ratio (W1/W2)	L (mm)	h (μm)	A ($\times 10^{-9} \text{ m}^2$)
Rectangle	1.19	1.19	1			10.6
Trapezoid	2.02	1.05	1.96	2	8.7	9.13
Triangle	1.4	0.27	5.18			2.39

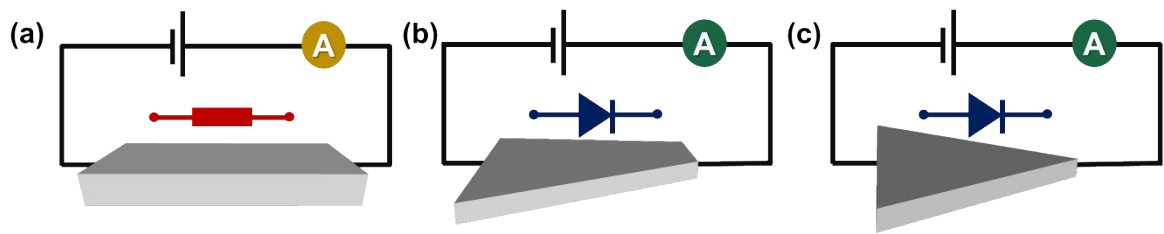


Fig. S18. Illustrations depicting the ion transport properties in the (a) symmetric rectangular, and asymmetric (b) trapezoidal and (c) triangular MXA membranes. Ions preferentially moves from the bottom side to tip side of a trapezoidal (or triangular) membrane.

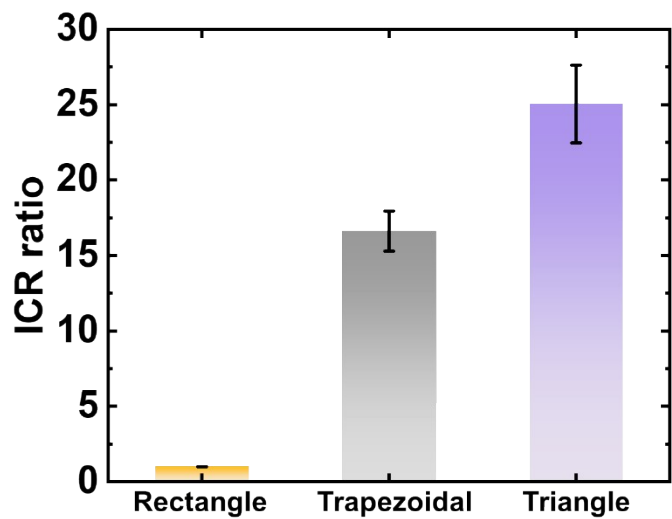


Fig. S19. The effect of MXA membrane geometry on nanofluidic rectification ratio.

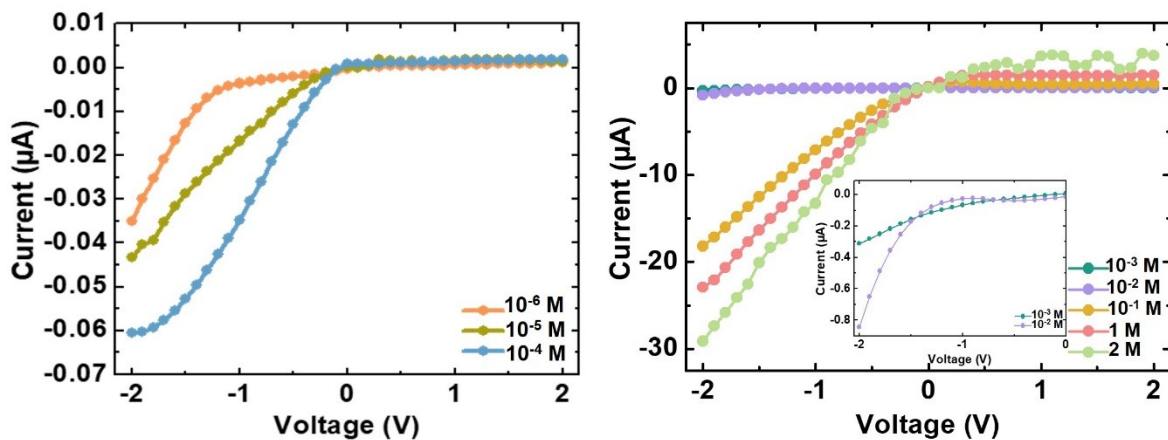


Fig. S20. Representative I-V curves of trapezoidal MXA_3 at various electrolyte concentrations.

Inset depicts the magnified results at 10^{-2} and 10^{-3} M.

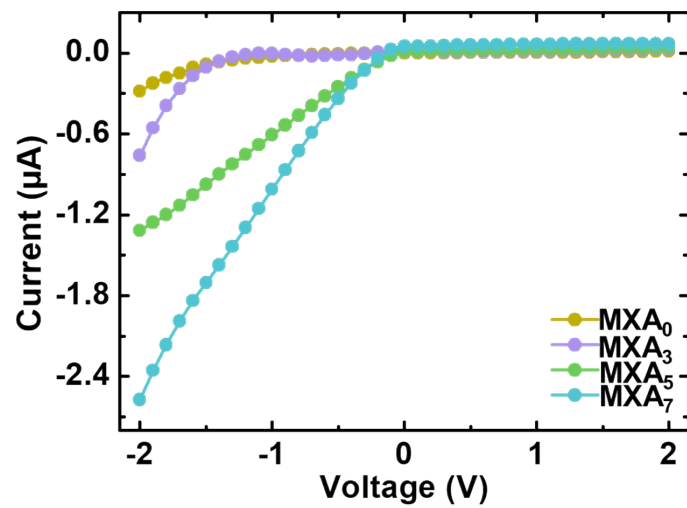


Fig. S21. Scanned I-V curves of MXA_x membranes with various ANF contents.

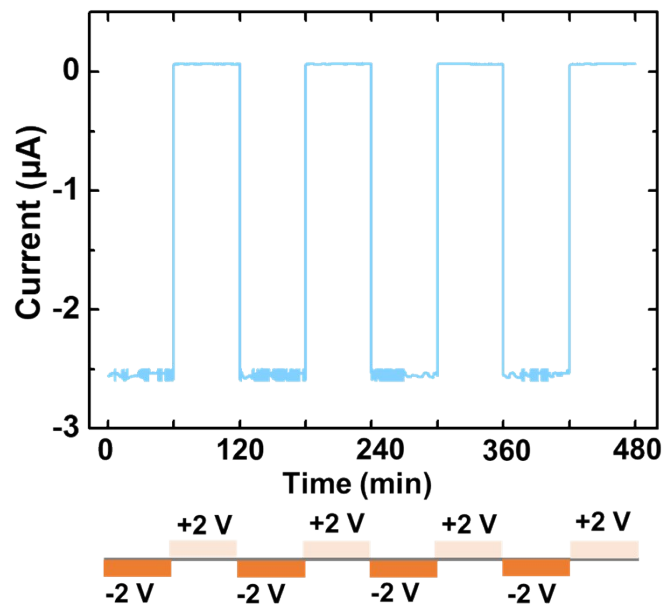


Fig. S22. Dynamic measurement of a MXA₇ membrane in 10 mM KCl, indicating its excellent ion transport stability.

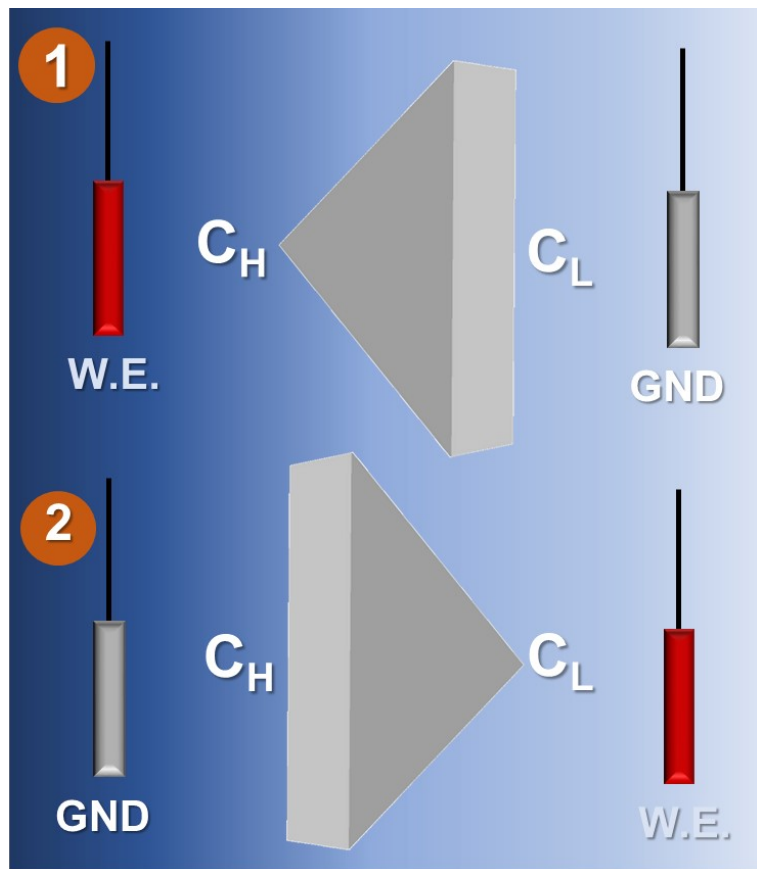


Fig. S23. Two tested arrangements for determining the preferential ion transport direction of the asymmetric MXA membrane.

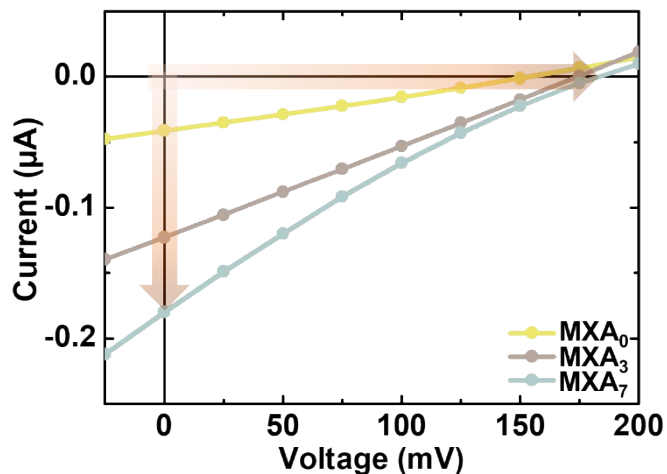


Fig. S24. Influence of the ANF content on the osmotic energy conversion of symmetric MXA_x membranes tested under a 50 mM/1 mM NaCl concentration gradient.

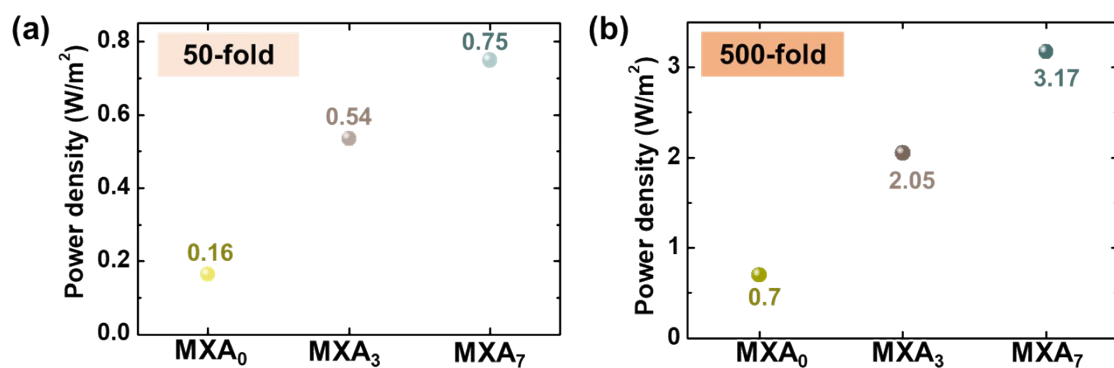


Fig. S25. The influence of the ANF content on the generated power densities of symmetric MXA_x membranes under (a) 50-fold (50 mM/1 mM) and (b) 500-fold (500 mM/1 mM) NaCl gradient.

Estimation of transference number of cations (t^+) and energy conversion efficiency (η_{\max})

To isolate the diffusion voltage (V_{diff}) and diffusion current (I_{diff}), the redox potential (V_{red}) contribution from the Ag/AgCl electrodes at varying concentration gradients was subtracted by applying a sweeping voltage from -0.4 to 0.4 V in 0.01 V increments using a non-selective micro-window hole (Fig. S38). This setup ensured that the measured voltage of V_{red} was solely attributed to the uneven redox reactions at the electrode-solution interfaces. In the nanofluidic osmotic energy conversion system, the generated V_{OC} is influenced by V_{diff} generated by the power source and the $V_{\text{red}}.$ ¹ This relationship is expressed as follows:

$$V_{\text{OC}} = V_{\text{diff}} + V_{\text{red}} \quad (\text{S2})$$

Thus, V_{diff} was calculated by subtracting V_{red} from V_{OC} , as described in Eq. (S3),

$$V_{\text{diff}} = V_{\text{OC}} - V_{\text{red}} \quad (\text{S3})$$

Upon obtaining V_{diff} , the transference number of cations (t^+) for the tested membrane can be calculated as follows:

$$t^+ = \frac{V_{\text{diff}}}{2 \left(\frac{RT}{F} \right) \ln \left(\frac{\gamma_H C_H}{\gamma_L C_L} \right)} + 0.5 \quad (\text{S4})$$

Here, R is the universal gas constant, T is the absolute temperature, F is the Faraday constant, γ_H and γ_L are the activities of the electrolytes in the high and low concentration sides, respectively, and C_H and C_L are the high and low electrolyte concentrations, respectively. Then, the energy conversion efficiency (η_{\max}), indicating the maximum power generation efficiency under a given concentration gradient, can be calculated using the following equation:

$$\eta_{\max} = \frac{(2t^+ - 1)^2}{2} \times 100\% \quad (\text{S5})$$

For the perfectly cation-selective membrane, t^+ reaches its maximum value of 1, resulting in a maximum energy conversion efficiency of 50%. The values of obtained V_{OC} , V_{red} , V_{diff} , t^+ , and η_{max} under various concentration gradients are provided in Table S3 and S5.

Table S3. A summary of the achieved V_{OC} , V_{red} , V_{diff} , t^+ , and η_{max} from a symmetrical MXA₇ membrane under two NaCl concentration gradients.

NaCl gradient (mM/mM)	V_{OC} (mV)	V_{red} (mV)	V_{diff} (mV)	t^+	η_{max} (%)
50/1	178	82.3	95.7	~1.00	~50.0
500/1	267	119	148	0.998	49.5

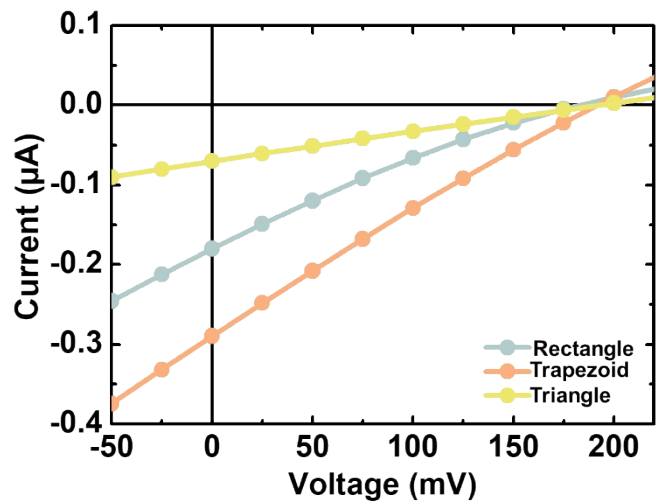


Fig. S26. Influence of the membrane geometry on the osmotic energy conversion of MXA_x membranes tested under a 50 mM/1 mM NaCl concentration gradient.

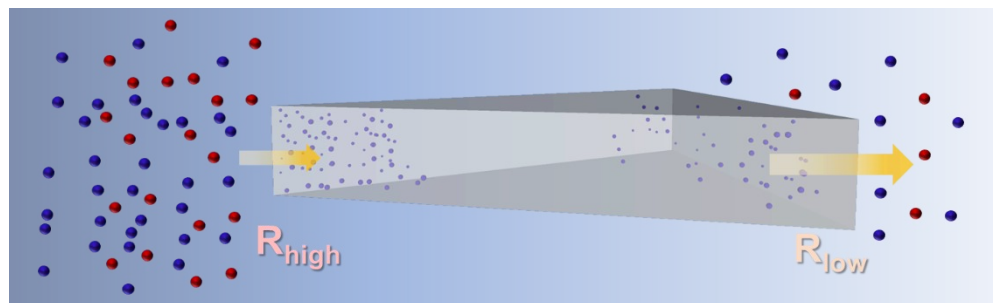


Fig. S27. Diagram illustrating ion diffusion in the presence of a concentration gradient through a triangular MXA membrane.

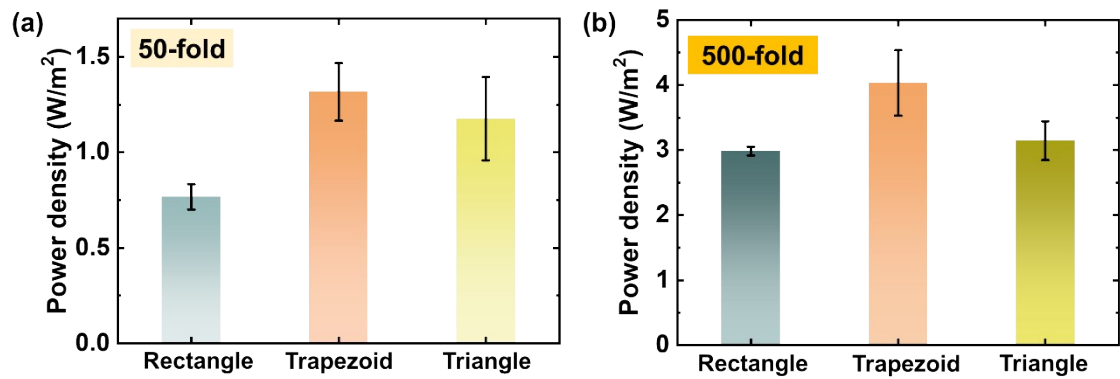


Fig. S28. The bar charts showing the power density of MXA₇ in relation to the membrane's geometry under both (a) 50 mM/1 mM and (b) 500 mM/1 mM NaCl gradients.

Table S4. Preparation of trapezoidal MXA₇ membranes with various axial lengths.

Membranes	Length (mm)
MXA ₇ (L ₁)	2.00
MXA ₇ (L ₂)	1.37
MXA ₇ (L ₃)	1.03
MXA ₇ (L ₄)	0.50

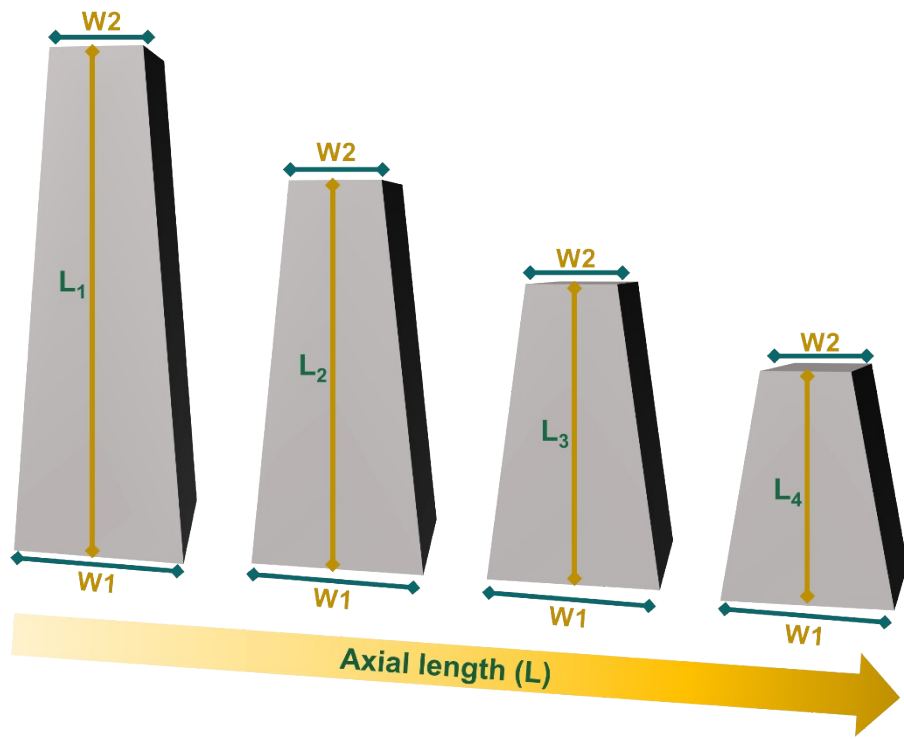


Fig. S29. Schematic diagram of trapezoidal MXA₇ membranes with various axial lengths (L).

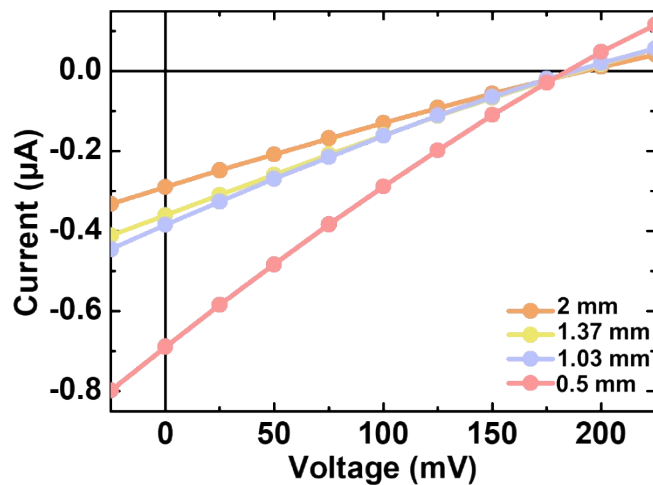


Fig. S30. Influence of the axial length of MXA₇ membranes on the osmotic energy conversion performance tested under a 50 mM/1 mM NaCl concentration gradient.

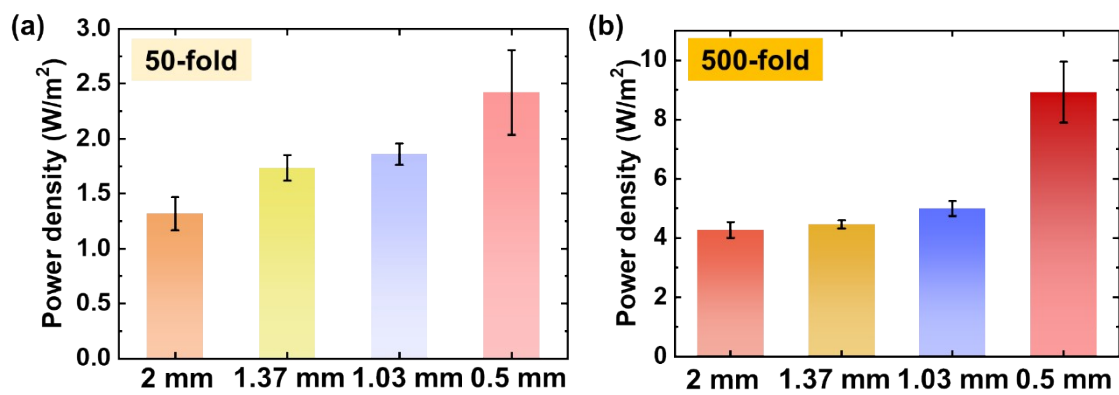


Fig. S31. The bar charts showing the power density of MXA₇ in relation to the membrane's axial length under both (a) 50 mM/1 mM and (b) 500 mM/1 mM NaCl gradients.

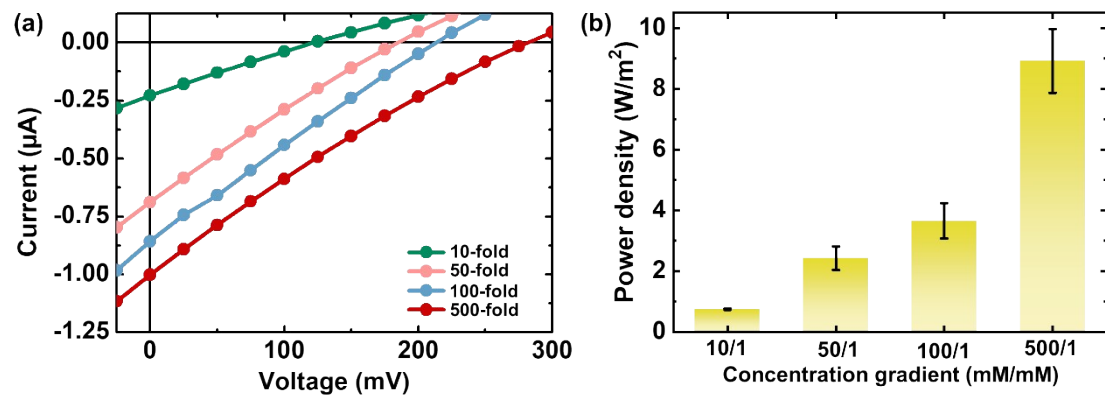


Fig. S32. Influence of the NaCl concentration gradient on the generated (a) I-V and (b) osmotic power density of a MXA₇ membrane. The low concentration was fixed at 1 mM.

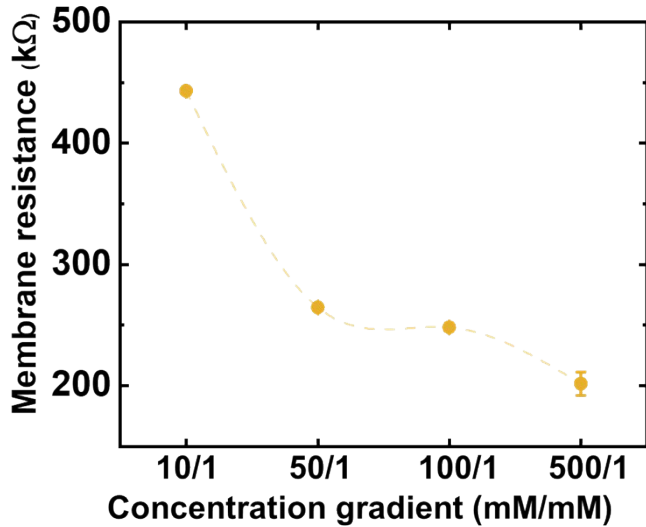


Fig. S33. The internal resistance of MXA₇ membranes as a function of concentration gradient.

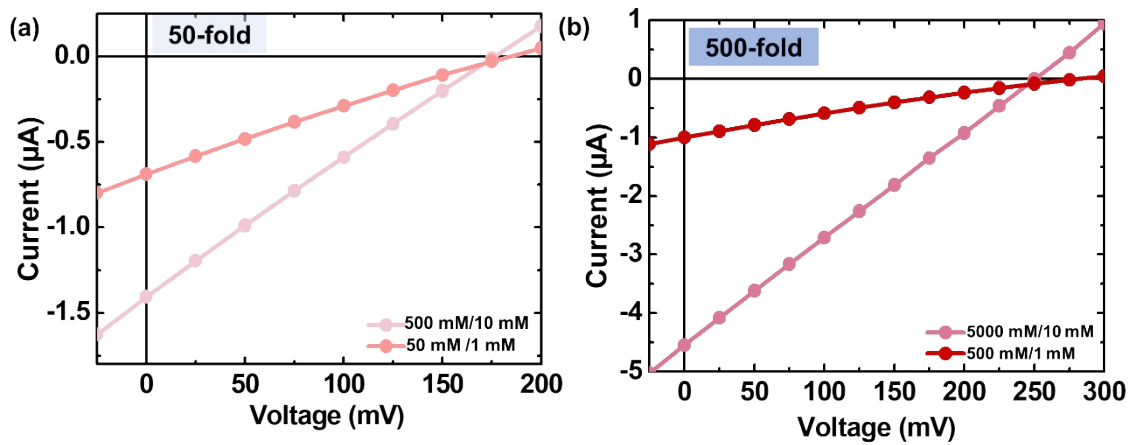


Fig. S34. Osmotic energy conversion performances of a MXA₇ membrane in response to the concentration gradients of (a) 50-fold and (b) 500-fold.

Table S5. A summary of the achieved V_{oc} , V_{red} , V_{diff} , t^+ , and η_{max} from a trapezoidal MXA₇ membrane under a 50-fold NaCl gradient.

NaCl gradient (mM/mM)	V_{oc} (mV)	V_{red} (mV)	V_{diff} (mV)	t^+	η_{max} (%)
500/10	175	84.7	90.3	0.999	~49.8

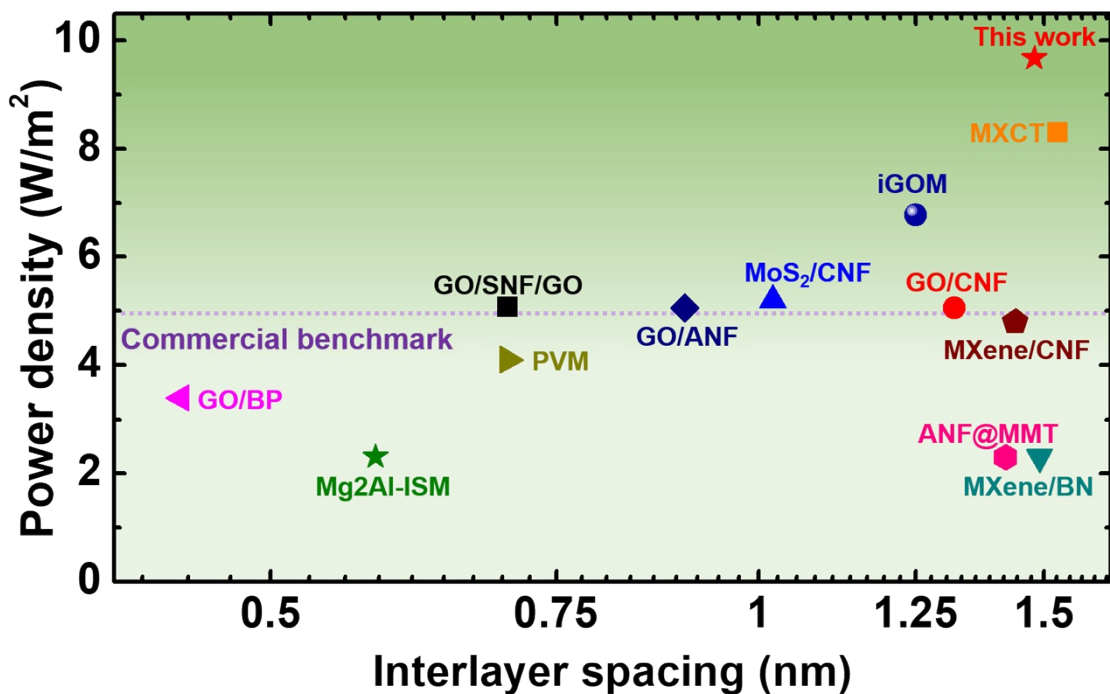


Fig. S35. The comparison of the achieved power densities of our designed asymmetric MXA membrane with reported 2D sub-nanofluidic membranes under the same 50-fold NaCl gradient.

Table S6. Comparison of the maximum output power density of the present MXA membrane with previously reported 2D single-layer sub-nanofluidic membranes under the same 500 mM/10 mM NaCl gradient.

2D membrane	Interlayer spacing (nm)	Power density (W/m ²)	Reference
ANF@MMT	1.42	2.3	2
MXene/CNF	1.44	4.8	3
GO/ANF	0.90	5.06	4
PVM	0.70	4.1	5
GO/BP	0.44	3.4	6
MXene/BN	1.49	2.3	7
Mg ₂ Al-ISM	0.58	2.31	8
MoS ₂ /CNF	1.02	5.2	9
GO/CNFs	1.32	5.06	10
GO/SNF/GO	0.70	5.07	11
iGOM	1.25	6.78	12
MXCT	1.53	8.29	13
MXA ₇	1.48	9.7	This work

Table S7. The comparison of the achieved transference number (t^+) and energy conversion efficiency (η_{\max}) between MXA and previously reported 2D materials-based membranes.

Membrane	Concentration gradient (mM/mM)	t^+	η_{\max} (%)	Reference
ANF@MMT	500/10	0.75	12.72	²
MXene/CNF	500/10	0.71	8.82	³
MXene/BN	500/10	0.88	29.4	⁷
MoS ₂ /CNF	500/10	0.873	27.83	⁹
iGOM	500/10	0.765	14.1	¹²
Cu-TCPP@SNF	500/10	0.743	11.8	¹⁴
MXene/PS-b-P2VP	500/10	0.813	19.59	¹⁵
MXene/ZIF-8	500/10	0.91	32.97	¹⁶
MXA ₇	500/10	0.999	49.8	This work

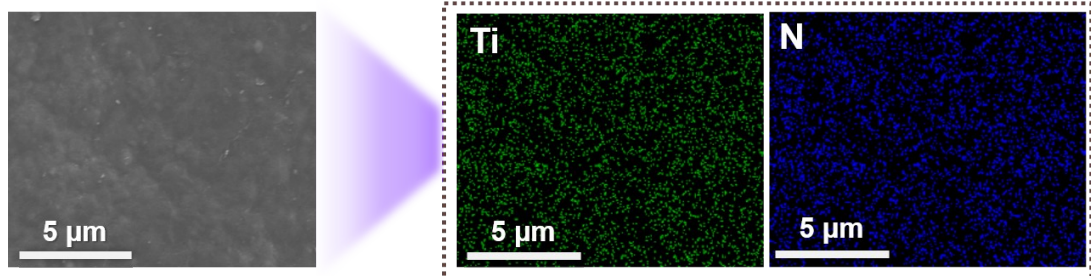


Fig. S36. The corresponding elemental EDX mapping analyses still can vividly detect the two main elements of Ti and F, manifesting the high stability of MXA membrane in high 0.5 M NaCl concentration.

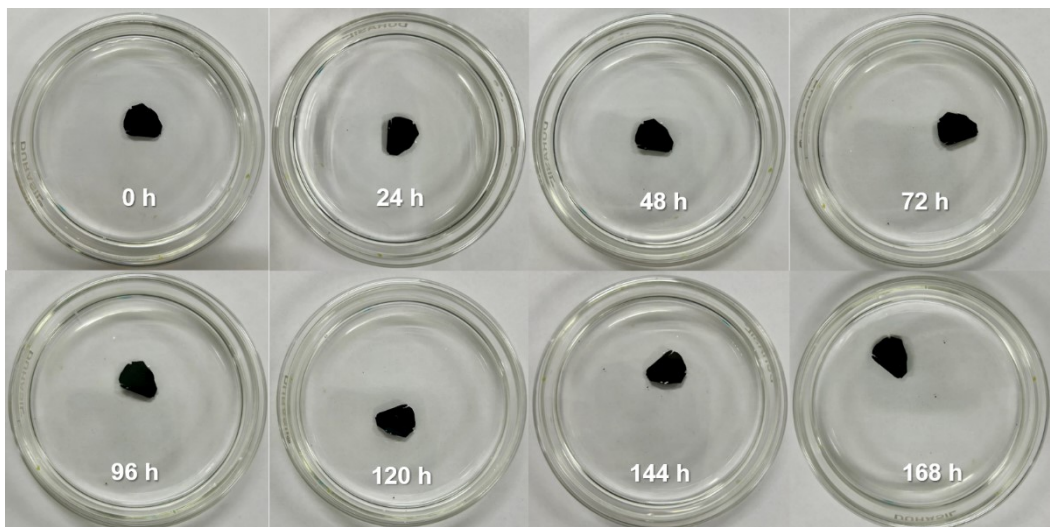


Fig. S37. Digital images of the MXA membrane immersed in water from 0 to 168 hours, demonstrating that the MXA maintains high structural stability in the working solvent.

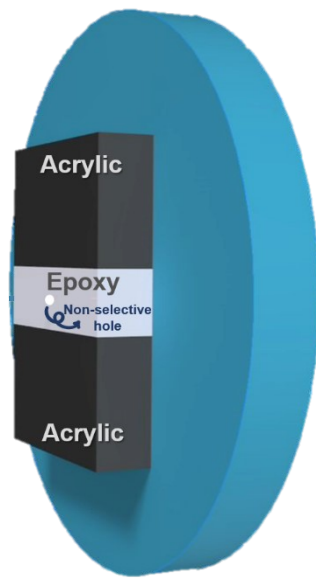


Fig. S38. Epoxy-acrylic device with non-selective hole for electrode calibration.

References

1. K. T. Huang, W. H. Hung, Y. C. Su, Y. C. Tang, L. D. Linh, C. J. Huang and L. H. Yeh, *Adv. Funct. Mater.*, 2023, **33**, 2211316.
2. R. Qin, J. Tang, C. Wu, Q. Zhang, T. L. Xiao, Z. Liu, Y. Jin, J. Liu and H. Wang, *Nano Energy*, 2022, **100**, 107526.
3. P. Liu, T. Zhou, L. S. Yang, C. C. Zhu, Y. F. Teng, X. Y. Kong and L. P. Wen, *Energy Environ. Sci.*, 2021, **14**, 4400-4409.
4. J. J. Chen, W. W. Xin, W. P. Chen, X. L. Zhao, Y. C. Qian, X. Y. Kong, L. Jiang and L. P. Wen, *ACS Central Sci.*, 2021, **7**, 1486-1492.
5. L. Cao, H. Wu, C. Y. Fan, Z. M. Zhang, B. B. Shi, P. F. Yang, M. Qiu, N. A. Khan and Z. Y. Jiang, *J. Mater. Chem. A*, 2021, **9**, 14576-14581.
6. Z. Zhang, P. P. Zhang, S. Yang, T. Zhang, M. Loffler, H. H. Shi, M. R. Lohe and X. L. Feng, *Proc. Natl. Acad. Sci. U.S.A.*, 2020, **117**, 13959-13966.
7. G. L. Yang, D. Liu, C. Chen, Y. J. Qian, Y. Y. Su, S. Qin, L. Z. Zhang, X. G. Wang, L. Sun and W. W. Lei, *ACS Nano*, 2021, **15**, 6594-6603.
8. S. Qin, G. L. Yang, S. A. Wang, Y. X. Ma, Z. Y. Wang, L. F. Wang, D. Liu and W. W. Lei, *Small*, 2024, **20**, 2400850.
9. C. C. Zhu, P. Liu, B. Niu, Y. N. Liu, W. W. Xin, W. P. Chen, X. Y. Kong, Z. Zhang, L. Jiang and L. P. Wen, *J. Am. Chem. Soc.*, 2021, **143**, 1932-1940.
10. Y. D. Wu, W. W. Xin, X. Y. Kong, J. J. Chen, Y. C. Qian, Y. Sun, X. L. Zhao, W. P. Chen, L. Jiang and L. P. Wen, *Mater. Horiz.*, 2020, **7**, 2702-2709.
11. W. W. Xin, H. Y. Xiao, X. Y. Kong, J. J. Chen, L. S. Yang, B. Niu, Y. C. Qian, Y. F. Teng, L. Jiang and L. P. Wen, *ACS Nano*, 2020, **14**, 9701-9710.
12. P. P. Yan, X. C. Chen, Z. X. Liang, Y. P. Fang, J. M. Yao, C. X. Lu, Y. R. Cai and L. Jiang, *Small*, 2023, **19**, 2205003.
13. W. H. Lin, T. Y. Huang, C. H. Bai, C. H. Hung, C. A. Lung, W. H. Hung, K. Gopinadhan and L. H. Yeh, *Nano Energy*, 2024, **128**, 109924.
14. V. P. Mai, C. R. Gu, A. R. Fauziah, Z. J. Yang, K. C. W. Wu, L. H. Yeh and R. J. Yang, *Chem. Eng. J.*, 2024, **484**, 149649.
15. X. B. Lin, P. Liu, W. W. Xin, Y. F. Teng, J. J. Chen, Y. D. Wu, Y. F. Zhao, X. Y. Kong, L. Jiang and L. P. Wen, *Adv. Funct. Mater.*, 2021, **31**, 2105013.
16. J. Zhou, J. Hao, R. Wu, L. Su, J. Wang, M. Qiu, B. Bao, C. Ning, C. Teng, Y. Zhou and L. Jiang, *Adv. Funct. Mater.*, 2022, **32**, 2209767.